Highlights

Size effects in a power law creeping layer under compression or shear, and implications for deformation mechanisms of lithium films

Alessandro Leronni, Vikram S. Deshpande, Norman A. Fleck

- A strain gradient viscoplasticity theory for size effects in creeping metal layers
- Assessment of relative roles of plastic constraint and size effect on layer strength
- Validation against tests on lithium films by suitable choice of material length scale

Size effects in a power law creeping layer under compression or shear, and implications for deformation mechanisms of lithium films

Alessandro Leronni, Vikram S. Deshpande, Norman A. Fleck*

Cambridge University Engineering Department,
Trumpington Street, Cambridge, CB2 1PZ, UK

Abstract

The axisymmetric compression of a power law creeping metallic sandwich layer of micron-scale thickness is analysed. Account is taken of the elevation in flow strength due to the presence of a spatial gradient in plastic strain rate. Numerical and analytical solutions reveal that the average compressive traction is enhanced by a combination of strain rate gradients and plastic constraint. A similar size effect is predicted for simple shear of the creeping sandwich layer. The difference in responses for compression and shear is traced to the different profiles of shear strain rate through the thickness of the layer. The sensitivity of compressive and shear strengths to the choice of higher-order boundary condition is explored, and good agreement with recent experiments on compression and shear of a thin sandwich layer of lithium is achieved by assuming fully clamped higher-order boundary conditions and a material length scale on the order of $3\,\mu$m in the strain gradient-based creep theory.

*Corresponding author
Email address: naf1@cam.ac.uk (Norman A. Fleck)

Preprint submitted to Journal of the Mechanics and Physics of Solids September 1, 2023

Keywords: creep, dislocations, strengthening and mechanisms, metallic materials, strain gradient plasticity

1. Introduction

Size effects arising from strain gradients in glide plasticity are well established both experimentally and theoretically. The presence of geometrically necessary dislocations, associated with a gradient in plastic strain, elevates the flow strength (Ashby, 1970; Fleck et al., 1994). In contrast, the degree to which spatial gradients of plastic strain rate influence the flow strength of a creeping metal remains poorly understood. Iliev et al. (2017) observed a size effect both in bending and indentation of indium at room temperature, and they explained the elevation in creep strength in terms of the spatial gradient in strain rate. By making use of rate dependent, phenomenological strain gradient theory (Hutchinson and Fleck, 1997), they inferred a material length scale of approximately 100 microns, which is two orders of magnitude greater than that for rate independent plasticity of structural alloys.

The purpose of the present study is to investigate a recently observed size effect in power law creep of lithium for two geometries of practical interest in solid state lithium ion batteries: constrained compression and constrained shear (Stallard et al., 2023). It is generally accepted that bulk specimens of lithium at room temperature deform by power law creep when the strain rate is in the range of $10^{-8}\,\mathrm{s}^{-1}$ to $10^{-2}\,\mathrm{s}^{-1}$ (Sargent and Ashby, 1984), such that the true stress σ in uniaxial tension scales with the true strain rate $\dot{\varepsilon}$ by

$$\frac{\sigma}{\sigma_0} = \left(\frac{\dot{\varepsilon}}{\dot{\varepsilon}_0}\right)^M \tag{1}$$

where $(\sigma_0, \dot{\varepsilon}_0)$ are material constants and M is the creep exponent. Bulk measurements on lithium suggest that $\sigma_0 = 1\,\text{MPa}$ and $M = 1/6.55$, for the choice $\dot{\varepsilon}_0 = 10^{-3}\,\text{s}^{-1}$ (LePage et al., 2019; Masias et al., 2019; Fincher et al., 2020).

We proceed to summarise the size effects that have been observed for lithium specimens of characteristic dimension on the order of microns and below. The pillar compression tests of Xu et al. (2017) found that the yield strength of lithium increases from 15 MPa to 105 MPa as the pillar diameter decreases from $9.5\,\mu$m to $1.39\,\mu$m. Fincher et al. (2020) reported that the hardness of lithium increases from 7.5 MPa at an indentation depth of $10\,\mu$m to 43 MPa at an indentation depth of 250 nm, for a representative strain rate of $0.05\,\text{s}^{-1}$ in the indentation test. In consistent manner, Herbert et al. (2018) found that lithium can support an average indentation pressure of 23 MPa to 175 MPa at an indentation depth of 40 nm, as the indentation strain rate increases from $0.20\,\text{s}^{-1}$ to $1.36\,\text{s}^{-1}$.

Recently, Stallard et al. (2023) performed compression and shear tests on a thin lithium layer sandwiched between ceramic substrates in order to mimic the mechanical environment experienced by micron-scale lithium filaments (or 'dendrites') that develop during the cracking of a ceramic electrolyte in a solid state battery (Janek and Zeier, 2016; Cheng et al., 2017; Kasemchainan et al., 2019; Kazyak et al., 2020; Shishvan et al., 2020; Ning et al., 2021; Mukherjee et al., 2023; Ning et al., 2023).

We begin by briefly reviewing the compression tests by Stallard et al. (2023) on thin cylindrical lithium layers of radius a and height h. The layers were sandwiched between quartz plates and the plates were subjected to an approach rate v that varied during the tests such that the through-thickness true strain rate was held fixed at $v/h = 10^{-3}\,\mathrm{s}^{-1}$, see Fig. 1(a). Stallard et al. (2023) plotted the average pressure on the film $\bar{p}$ as a function of a/h. They accounted for the role of plastic constraint at large a/h in elevating the average pressure by making use of the analytical solution of Cheng et al. (2017) for the compression of a power law creeping film. Using this solution they deduced that the value of σ_0 increased from a bulk value of 1 MPa at $h = 200\,\mu\mathrm{m}$ to 2 MPa at $h = 15\,\mu\mathrm{m}$, see their Fig. 7(c).

Stallard et al. (2023) also performed shear experiments on sandwiched circular cylindrical lithium layers by applying a tangential velocity v to the top plate while holding fixed the bottom plate, see Fig. 1(b). They were careful to perform the shear tests at a value of von Mises strain rate equal to $10^{-3}\,\mathrm{s}^{-1}$, consistent with their compression tests. They measured the average shear traction on their specimens and converted it to an equivalent von Mises stress in the usual manner. By so doing, they found that the value of σ_0 increased from 1 MPa at $h = 200\,\mu\mathrm{m}$ to 1.3 MPa at $h = 24\,\mu\mathrm{m}$.

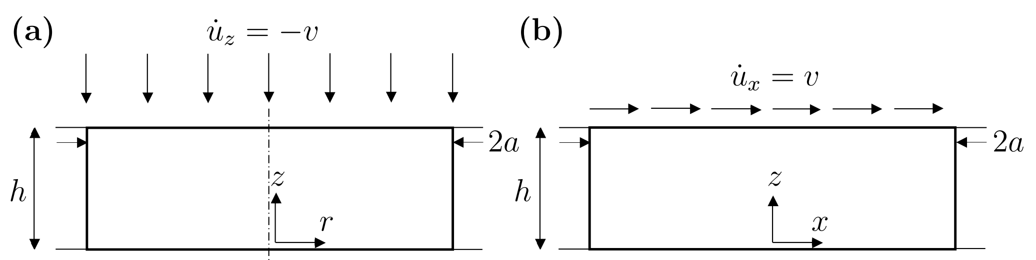

Fig. 1: Axisymmetric compression and simple shear of sandwiched lithium layers of radius a and height h, adapted from Stallard et al. (2023). **(a)** Axisymmetric compression, such that an axial velocity $\dot{u}_z = -v$ is applied to the top face of the layer, and **(b)** simple shear, such that a tangential velocity $\dot{u}_x = v$ is applied to the top face of the layer.

In the present study, strain gradient plasticity theory is used to predict the observed size effect of Stallard et al. (2023) for sandwiched thin lithium layers subjected to compression and shear, and thereby give a mechanistic interpretation of size effect that can exist in addition to strengthening by plastic constraint. Specifically, lithium is treated as a rigid, power law creeping solid (Wang and Cheng, 2017; LePage et al., 2019; Masias et al., 2019; Fincher et al., 2020). A phenomenological, isotropic theory of rate dependent strain gradient plasticity is used such that an overall effective plastic strain rate is defined in terms of the von Mises plastic strain rate and a scalar measure of plastic strain rate gradient along with a single material length scale (Fleck and Willis, 2009; Niordson and Hutchinson, 2011). Numerical solutions are obtained via the finite element method. Analytical upper bound solutions are also reported by assuming a suitable velocity field, analogous to the approach of Niordson and Hutchinson (2011) for constrained compression in plane strain for a rate independent solid.

The present paper builds upon previous experiments and analyses of constrained compression and shear of a thin, rate independent solid. For example, Mu et al. (2014) measured the compression and shear responses of a thin copper layer confined between chromium nitride substrates and also silicon substrates. They observed a significant size effect in both compression and shear: the average compressive stress for a layer thickness of 550 nm is twice that for a thickness of 1.18 μm, and the average shear stress for a thickness of 150 nm is twice that for a thickness of 1.18 μm.

Mu et al. (2014) used a phenomenological strain gradient plasticity theory to predict the compression and shear responses of their copper specimens.

They treated the copper as a rigid-perfectly plastic solid, assumed that plastic flow is fully constrained at the layer/substrate interfaces and chose a material length scale of 647 nm to match the measured average shear stress for a layer thickness of 550 nm. However, their model overestimates the enhancement in both compressive and shear strength for the thinner layers.

The shear strength of the confined copper layer of Mu et al. (2014, 2016) has also been analysed by the one-dimensional strain gradient plasticity model of Kuroda and Needleman (2019, 2023). They assumed that the plastic shear strain gradient at the layer/substrate interface cannot exceed a limiting value. This limit on strain gradient at the boundary has also been assumed by Kuroda et al. (2021) in their finite element analyses of elastic-plastic thin metal layers confined between elastic solids. This enrichment of the strain gradient model led to good agreement with the shear and compression experiments of Mu et al. (2014, 2016). Alternatively, Dahlberg and Ortiz (2019) were able to reproduce the results of the constrained shear experiments of Mu et al. (2014, 2016) by introducing fractional derivatives of plastic strain into their phenomenological strain gradient plasticity theory. Both the phenomenological models of Kuroda and Needleman (2019, 2023) and of Dahlberg and Ortiz (2019) highlight the significance of the higher-order boundary condition in influencing the size effect. Danas et al. (2010) gave a micromechanical interpretation of the role of the higher-order boundary condition by replacing the interface with a compliant elastic interphase that dictates the degree of build-up of back-stress to dislocation pile-ups.

The outline of the present paper is as follows. The phenomenological, rate dependent strain gradient plasticity theory is summarised in Section 2.

This theory is specialised for two-dimensional, axisymmetric compression in Section 3, and for one-dimensional shear in Section 4. Numerical solutions and approximate analytical solutions based on an assumed velocity field are given for both compression and shear. Comparison between theory and experiment on lithium layers is given in Section 5, and a concluding discussion is reported in Section 6.

2. Theoretical framework

The principle of virtual power is used to obtain the field equations for the proposed rate dependent strain gradient plasticity theory. The theory makes use of the full tensor theory of Fleck and Willis (2009) but considers a version involving a single material length scale on the grounds of simplicity.

The approach is to write the total strain rate tensor $\dot{\varepsilon}_{ij}$ in the current configuration x_i as the sum of an elastic rate $\dot{\varepsilon}^{\mathrm{e}}_{ij}$ and a viscoplastic rate $\dot{\varepsilon}^{\mathrm{p}}_{ij}$, such that $\dot{\varepsilon}_{ij} = \dot{\varepsilon}^{\mathrm{e}}_{ij} + \dot{\varepsilon}^{\mathrm{p}}_{ij}$. The internal work rate per unit current volume includes a gradient term $\dot{\varepsilon}^{\mathrm{p}}_{ij,k} = \partial\dot{\varepsilon}^{\mathrm{p}}_{ij}/\partial x_k$ in order to develop a strain gradient theory. The problems under consideration involve creep rates that far exceed the elastic strain rates and consequently elasticity can be neglected. Large changes in geometry occur but it suffices to solve for the velocity field $\dot{u}_i(x_j)$ in the current configuration for any given aspect ratio a/h of specimen. As deformation proceeds a/h evolves and the macroscopic load is determined as a function of prescribed velocity.

Three stress measures enter the statement of internal virtual power: the Cauchy stress tensor σ_{ij}, a deviatoric stress tensor q_{ij} and a deviatoric higher-order stress tensor τ_{ijk} that are work-conjugate to the elastic strain rate tensor $\dot{\varepsilon}^{\mathrm{e}}_{ij}$, the deviatoric viscoplastic strain rate tensor $\dot{\varepsilon}^{\mathrm{p}}_{ij}$ and the gradient of deviatoric viscoplastic strain rate tensor $\dot{\varepsilon}^{\mathrm{p}}_{ij,k}$, respectively. The internal virtual power $\delta\dot{W}_{\mathrm{int}}$ in the current volume Ω, associated with the virtual fields $\delta\dot{\varepsilon}^{\mathrm{e}}_{ij}$, $\delta\dot{\varepsilon}^{\mathrm{p}}_{ij}$ and $\delta\dot{\varepsilon}^{\mathrm{p}}_{ij,k}$, is given by

$$\delta\dot{W}_{\mathrm{int}} = \int_{\Omega} \left(\sigma_{ij}\delta\dot{\varepsilon}^{\mathrm{e}}_{ij} + q_{ij}\delta\dot{\varepsilon}^{\mathrm{p}}_{ij} + \tau_{ijk}\delta\dot{\varepsilon}^{\mathrm{p}}_{ij,k} \right) \mathrm{d}V \tag{2}$$

It is convenient to write the Cauchy stress tensor in terms of a deviatoric component σ'_{ij} and a hydrostatic component $-p\delta_{ij}$, where p is pressure and δ_{ij} denotes the usual second-order identity tensor, such that $\sigma_{ij} = \sigma'_{ij} - p\delta_{ij}$. Then, the internal virtual power can be rephrased as

$$\delta\dot{W}_{\mathrm{int}} = \int_{\Omega} \left[\sigma_{ij}\delta\dot{\varepsilon}_{ij} + \left(q_{ij} - \sigma'_{ij} \right) \delta\dot{\varepsilon}^{\mathrm{p}}_{ij} + \tau_{ijk}\delta\dot{\varepsilon}^{\mathrm{p}}_{ij,k} \right] \mathrm{d}V \tag{3}$$

Upon relating the strain rate tensor to the velocity field $\dot{u}_i$ such that $\dot{\varepsilon}_{ij} = \left(\dot{u}_{i,j} + \dot{u}_{j,i} \right)/2$ and upon making use of the divergence theorem, we obtain

$$\begin{aligned} \delta\dot{W}_{\mathrm{int}} = \int_{\Omega} & \left[-\sigma_{ij,j}\delta\dot{u}_i + \left(q_{ij} - \tau_{ijk,k} - \sigma'_{ij} \right) \delta\dot{\varepsilon}^{\mathrm{p}}_{ij} \right] \mathrm{d}V \\ & + \int_{\partial\Omega} \left(\sigma_{ij}n_j\delta\dot{u}_i + \tau_{ijk}n_k\delta\dot{\varepsilon}^{\mathrm{p}}_{ij} \right) \mathrm{d}A \end{aligned} \tag{4}$$

where n_i denotes the outward unit normal to the boundary $\partial\Omega$ of the current domain Ω. The external virtual power $\delta\dot{W}_{\mathrm{ext}}$ is expressed in terms of the usual traction T_i and a higher-order traction t_{ij} such that

$$\delta\dot{W}_{\mathrm{ext}} = \int_{\partial\Omega} \left(T_i\delta\dot{u}_i + t_{ij}\delta\dot{\varepsilon}^{\mathrm{p}}_{ij} \right) \mathrm{d}A \tag{5}$$

Upon invoking the principle of virtual power $\delta\dot{W}_{\mathrm{int}} = \delta\dot{W}_{\mathrm{ext}}$ for any virtual fields $\delta\dot{u}_i$ and $\delta\dot{\varepsilon}^{\mathrm{p}}_{ij}$, pointwise equilibrium in the current domain follows immediately as

$$\sigma_{ij,j} = \left(\sigma'_{ij} - p\delta_{ij} \right)_{,j} = 0 \tag{6a}$$

and

$$\sigma'_{ij} = q_{ij} - \tau_{ijk,k} \tag{6b}$$

along with the following traction relations on the boundary of the current domain:

$$T_i = \sigma_{ij} n_j \tag{7a}$$

and

$$t_{ij} = \tau_{ijk} n_k \tag{7b}$$

We emphasise that either the velocity field $\dot{u}_i$ or the traction T_i can be specified pointwise on the domain boundary. Higher-order boundary conditions are also imposed: either the plastic strain rate tensor $\dot{\varepsilon}_{ij}^{\mathrm{p}}$ or the higher-order traction t_{ij} is prescribed pointwise on the boundary.

Now consider a gradient formulation for a rigid, power law creeping solid. Elastic strains are neglected, and the viscoplastic strain rate tensor is directly related to the velocity field via

$$\dot{\varepsilon}_{ij} = \dot{\varepsilon}_{ij}^{\mathrm{p}} = \left(\dot{u}_{i,j} + \dot{u}_{j,i}\right)/2 \tag{8}$$

In the subsequent analysis we shall drop the superscript "p" from strain rate and strain rate gradient in order to simplify the notation. An overall effective (viscoplastic) strain rate $\dot{E}_{\mathrm{p}}$ is introduced, and includes a term in strain rate gradient along with a single plastic length scale l:

$$\dot{E}_{\mathrm{p}}^2 = 2\left(\dot{\varepsilon}_{ij}\dot{\varepsilon}_{ij} + l^2 \dot{\varepsilon}_{ij,k}\dot{\varepsilon}_{ij,k}\right)/3 \tag{9}$$

We note in passing that, in general, three invariants of $\dot{\varepsilon}_{ij,k}$ exist for an isotropic solid, with three associated length scales, see Smyshlyaev and Fleck

(1996). Eq. (9) is one simple version of the more general theory. Next, a creep potential U_{p} is introduced in the form of a power law in $\dot{E}_{\mathrm{p}}$ such that

$$U_{\mathrm{p}}(\dot{E}_{\mathrm{p}}) = \frac{\sigma_0 \dot{\varepsilon}_0}{M+1} \left(\frac{\dot{E}_{\mathrm{p}}}{\dot{\varepsilon}_0} \right)^{M+1} \tag{10}$$

where σ_0 is a reference stress value, $\dot{\varepsilon}_0$ is a reference strain rate value and M is the creep exponent, such that $0 \leq M \leq 1$. An overall effective stress Σ, work-conjugate to $\dot{E}_{\mathrm{p}}$, is obtained by differentiation of U_{p} with respect to $\dot{E}_{\mathrm{p}}$:

$$\Sigma = \frac{\partial U_{\mathrm{p}}}{\partial \dot{E}_{\mathrm{p}}} = \sigma_0 \left(\frac{\dot{E}_{\mathrm{p}}}{\dot{\varepsilon}_0} \right)^{M} \tag{11}$$

In similar fashion, the deviatoric stress tensor q_{ij}, work-conjugate to $\dot{\varepsilon}_{ij}$, and the deviatoric higher-order stress tensor τ_{ijk}, work-conjugate to $\dot{\varepsilon}_{ij,k}$, are obtained by differentiation of U_{p} with respect to $\dot{\varepsilon}_{ij}$ and $\dot{\varepsilon}_{ij,k}$, respectively, such that

$$q_{ij} = \frac{\partial U_{\mathrm{p}}}{\partial \dot{\varepsilon}_{ij}} = \frac{2}{3} \frac{\Sigma}{\dot{E}_{\mathrm{p}}} \dot{\varepsilon}_{ij} \tag{12a}$$

and

$$\tau_{ijk} = \frac{\partial U_{\mathrm{p}}}{\partial \dot{\varepsilon}_{ij,k}} = \frac{2}{3} l^2 \frac{\Sigma}{\dot{E}_{\mathrm{p}}} \dot{\varepsilon}_{ij,k} \tag{12b}$$

Note that for the case of uniaxial tension, in the absence of strain rate gradients, Σ reduces to the tensile stress σ, $\dot{E}_{\mathrm{p}}$ reduces to the uniaxial strain rate $\dot{\varepsilon}$ and Eq. (11) reduces to Eq. (1).

3. Axisymmetric compression problem

The strain gradient viscoplasticity theory presented in Section 2 is specialised to the case of axisymmetric compression of a cylindrical layer adhered to its substrates. A circular cylinder of radius a and height h is defined in

Fig. 1(a), along with a cylindrical coordinate system (r, θ, z) centred on the bottom face of the cylinder. The velocity components in the radial direction r and in the axial direction z are denoted by $\dot{u}_r$ and $\dot{u}_z$, respectively. The velocity $\dot{u}_z = -v$ is imposed on the top face of the cylinder, whereas the bottom face does not translate axially, $\dot{u}_z = 0$. No-slip is imposed between cylinder and substrates such that $\dot{u}_r = 0$ for all r along both $z = 0$ and $z = h$. The numerical solution is obtained by using the commercial finite element software COMSOL MultiPhysics.[1] Additional insight into the nature of the solution is achieved by making use of an upper bound approximate solution with an assumed velocity field, see Appendix A.

3.1. Numerical solution

The governing equations in the velocity field $\dot{u}_i$ are obtained by substitution of Eqs. (8)-(12) into Eqs. (6), and a solution is obtained by using COMSOL MultiPhysics. Quadratic finite elements are used for $\dot{u}_i$ and incompressibility is enforced by means of a Lagrange multiplier in the form of a pressure field $p(x_i)$; linear finite elements are used in order to describe the pressure field.

With reference to the geometry and reference system in Fig. 1(a), symmetry requires that $\dot{u}_r = 0$ and $\sigma_{rz} = 0$ on $r = 0$. The boundary at $r = a$ is traction-free such that $\sigma_{rr} = 0$ and $\sigma_{rz} = 0$. The boundary at $z = 0$ is fixed in the z-direction such that $\dot{u}_z = 0$, whereas $\dot{u}_z = -v$ is prescribed on $z = h$. Sticking boundary conditions are imposed on both $z = 0$ and $z = h$ such that $\dot{u}_r = 0$.

Higher-order boundary conditions are imposed in addition to the sticking

[1] https://www.comsol.com/, Version 5.6.

boundary conditions on the velocity component $\dot{u}_r$ tangential to the surface. Recall that the higher-order boundary term is of the form $\tau_{ijk} n_k \delta\dot{\varepsilon}_{ij}$, see Eq. (4). Symmetry at $r = 0$ dictates that $\tau_{rrr} = \tau_{\theta\theta r} = \tau_{zzr} = 0$ along with $\dot{\varepsilon}_{rz} = 0$. Traction-free higher-order stress on $r = a$ demands that $\tau_{rrr} = \tau_{\theta\theta r} = \tau_{zzr} = \tau_{rzr} = 0$. There remains a choice of higher-order boundary condition on $z = 0$ and $z = h$. We consider the two extremes of a fully *constrained* higher-order boundary condition $\dot{\varepsilon}_{rz} = 0$, and an *unconstrained* higher-order boundary condition such that $\tau_{rzz} = 0$. Constrained plastic strain corresponds to the blocking of dislocations at the boundary, while unconstrained plastic strain ($\tau_{rzz} = 0$) is the natural boundary condition associated with the free motion of dislocations into the boundary, see for example Shu et al. (2001).

The mesh has rectangular elements of number $10\,a/h$ in the r-direction, and 100 rectangular elements in the z-direction. For the constrained case, steep strain rate gradients exist near the boundaries at $z = 0$ and $z = h$. In order to capture these features in the numerical model, it is necessary to use a more refined mesh near the boundaries: the size of the largest element is twenty times that of the smallest element.

Selected aspects of the numerical solution are given in Fig. 2, for the choice $M = 1/7$ (a representative value for lithium, close to the value of $M = 1/6.55$ as observed by LePage et al., 2019, Masias et al., 2019 and Fincher et al., 2020) and for a large aspect ratio $a/h = 20$. The distributions of radial velocity $\dot{u}_r(z)$ and shear strain rate $\dot{\varepsilon}_{rz}(z)$ at $r/a = 1/2$ are plotted in Figs. 2(a) and (c), respectively, for the unconstrained case, and in Figs. 2(b) and (d), respectively, for the constrained case. The corresponding distribution

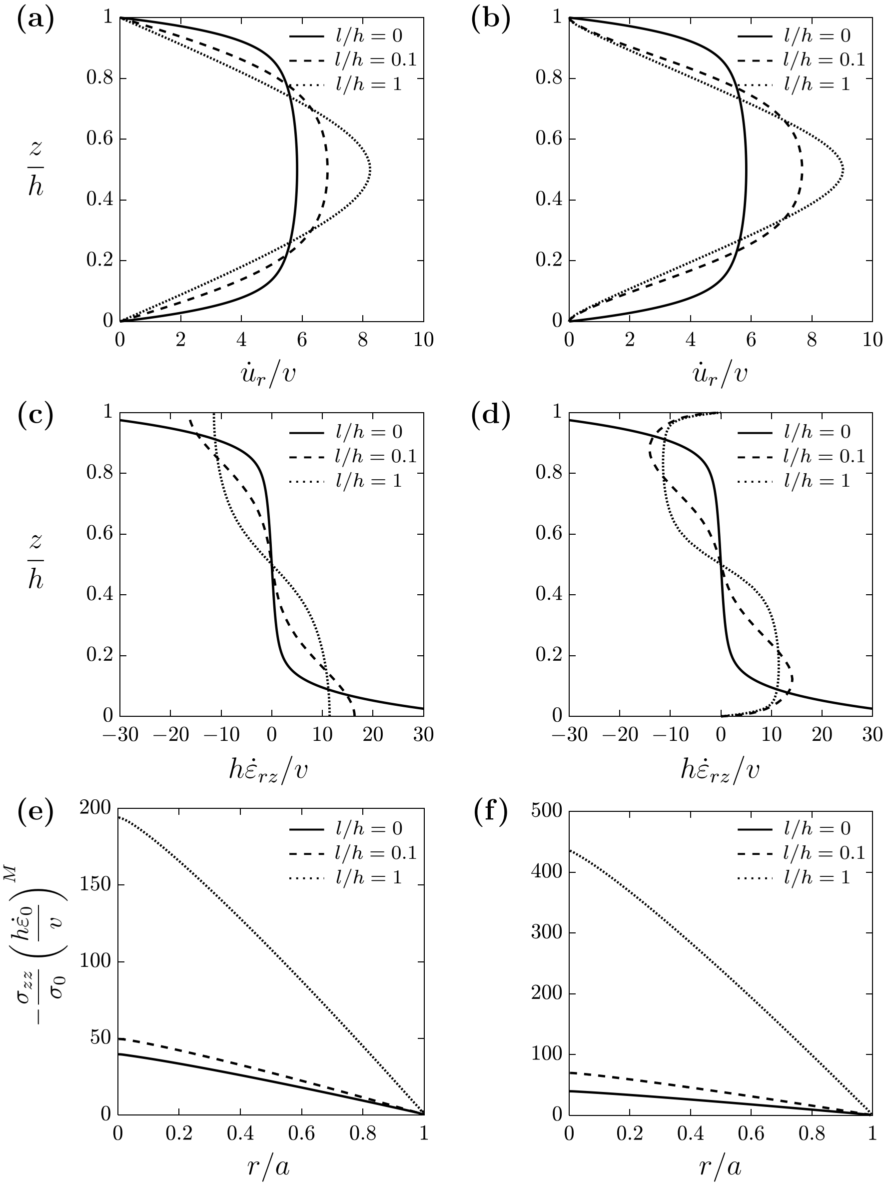

Fig. 2: Axisymmetric compression problem. Numerical solution for $M = 1/7$ and $a/h = 20$: $\dot{u}_r/v$ as a function of z/h for $r/a = 0.5$ in the **(a)** unconstrained and **(b)** constrained cases; $h\dot{\varepsilon}_{rz}/v$ as a function of z/h for $r/a = 0.5$ in the **(c)** unconstrained and **(d)** constrained cases; $-(\sigma_{zz}/\sigma_0)(h\dot{\varepsilon}_0/v)^M$ as a function of r/a on the plane $z/h = 1/2$ in the **(e)** unconstrained and **(f)** constrained cases. Solutions are plotted for selected values of l/h.

of axial stress $\sigma_{zz}(r)$ on the mid-plane $z/h = 1/2$ is given in Figs. 2(e) and (f) for the unconstrained and constrained cases, respectively. The sensitivity of response to l/h is shown by taking selected values of l/h from zero to unity in each plot; note that $l/h = 0$ is the limit of the conventional, power law creeping solid. The effect of invoking strain gradients in the creep theory with $l/h > 0$ is to give a more uniform shear strain rate through the thickness of the layer, see Fig. 2(c). The constrained higher-order boundary condition $\dot{\varepsilon}_{rz} = 0$ on $z/h = 0$ and $z/h = 1$ leads to a boundary layer of thickness on the order of l, see Fig. 2(d) for the case $l/h = 0.1$. An elevation in compressive strength of the layer with increasing l/h is evident in Figs. 2(e) and (f) for unconstrained and constrained higher-order boundary conditions, respectively. The imposition of a constrained higher-order boundary condition, $\dot{\varepsilon}_{rz} = 0$, also elevates the strength: for example, at $l/h = 1$, the peak value of axial stress at $r = 0$ for the constrained case is about twice that for the unconstrained case, compare Figs. 2(e) and (f).

The average pressure $\bar{p}$ is obtained as $\bar{p} = -(2/a^2)\int_0^a \sigma_{zz}(r, z = h/2)\, r\, \mathrm{d}r$. The numerical solution for $(\bar{p}/\sigma_0)(h\dot{\varepsilon}_0/v)^M$ is plotted in Fig. 3(a) as a function of l/h for $M = 1/7$, and for selected values of a/h, in the constrained and unconstrained cases. Note that $\bar{p}$ increases with increasing l/h and with increasing a/h, and is larger for the constrained case than for the unconstrained case. Analytical solutions have also been obtained by assuming a suitable velocity field, as detailed in Appendix A. These upper bound solutions overestimate the numerical solutions by less than 10%.

It is instructive to re-plot the results of Fig. 3(a) by normalising the average pressure $\bar{p}$ at finite l/h by the response for $l/h = 0$, again as a

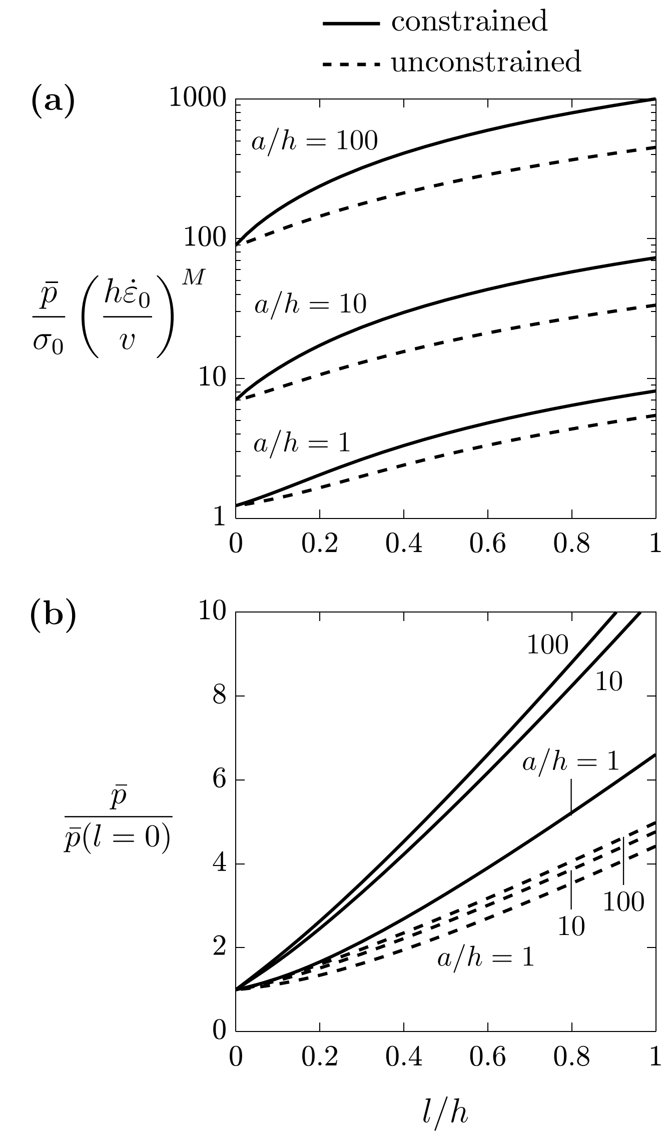

Fig. 3: Axisymmetric compression problem. Numerical solution for constrained and unconstrained higher-order boundary conditions: **(a)** $(\bar{p}/\sigma_0)(h\dot{\varepsilon}_0/v)^M$ and **(b)** $\bar{p}/\bar{p}(l=0)$ as a function of l/h for $M = 1/7$ and for selected values of a/h. The average pressure $\bar{p}$ is defined as the average of the axial stress on the mid-plane, that is, $\bar{p} = -(2/a^2)\int_0^a \sigma_{zz}(r, z = h/2)\, r\, \mathrm{d}r$.

function of l/h, see Fig. 3(b). For both constrained and unconstrained higher-order boundary conditions, this ratio increases with increasing a/h up to $a/h = 10$, but then attains a limiting value for $a/h > 10$. This observation suggests that, for large values of aspect ratio, the elevation in strength due to the size effect, associated with l/h, and the elevation in strength due to plastic constraint, associated with a/h, can be decoupled in a multiplicative manner. This is confirmed in the following section, where an asymptotic analytical solution at large a/h is reported.

3.2. Asymptotic solution for large aspect ratio $a/h \gg 1$

Accurate finite element solutions at large values of aspect ratio a/h are computationally expensive. Moreover, the derivation of an asymptotic solution for large aspect ratio allows us to shed light on the relative importance of plastic constraint and size effect on the sensitivity of compressive strength to layer thickness.

An upper bound solution for the average pressure is derived in Appendix A. Write $\bar{a} = a/h$ as the aspect ratio, and $\hat{r} = r/a$ and $\bar{z} = z/h$ as the non-dimensional cylindrical co-ordinates. Then, the upper bound solution is based upon an assumed velocity field of:

$$\frac{\dot{u}_r}{v} = \bar{a}\hat{r}\left[C_1\bar{z}(1-\bar{z}) + C_2\bar{z}^2(1-\bar{z})^2 + C_3\bar{z}^3(1-\bar{z})^3\right] \tag{13a}$$

and

$$\frac{\dot{u}_z}{v} = -2C_1\left(\frac{1}{2}\bar{z}^2 - \frac{1}{3}\bar{z}^3\right) - 2C_2\left(\frac{1}{3}\bar{z}^3 - \frac{1}{2}\bar{z}^4 + \frac{1}{5}\bar{z}^5\right) - 2C_3\left(\frac{1}{4}\bar{z}^4 - \frac{3}{5}\bar{z}^5 + \frac{1}{2}\bar{z}^6 - \frac{1}{7}\bar{z}^7\right) \tag{13b}$$

where C_1, C_2 and C_3 are scaling factors, to be determined by imposition of the boundary conditions and by minimisation of compressive load. An analogous displacement field has been proposed by Niordson and Hutchinson (2011) for the corresponding plane strain, rate independent problem.

As detailed in Appendix A, at large aspect ratio $\bar{a} \gg 1$, the average pressure can be written in non-dimensional fashion as Eq. (A.12), and repeated here as:

$$\frac{\bar{p}}{\sigma_0}\left(\frac{h\dot{\varepsilon}_0}{v}\right)^M = \frac{\bar{a}^{M+1}}{M+3}\min_{C_2}\left\{g_{\mathrm{c}}\left(C_2, M, \bar{l}\right)\right\} \tag{14}$$

where $\bar{l} = l/h$ and the function g_{c} to be minimised is given in Eq. (A.11) of Appendix A. Note from Eq. (14) that $(\bar{p}/\sigma_0)(h\dot{\varepsilon}_0/v)^M$ is multiplicatively decomposed into a contribution depending upon $\bar{a}$, quantifying the effect of plastic constraint, and a contribution depending upon $\bar{l}$, quantifying the role of size effect. Both contributions depend upon the creep exponent M.

The ratio of average pressure $\bar{p}$ given by Eq. (14) to the average pressure given by conventional rate dependent plasticity, $\bar{p}(l=0)$, is independent of $\bar{a}$. For illustration, this ratio is plotted in Fig. 4 as a function of l/h, for selected values of M. Predictions for the unconstrained case are given in Fig. 4(a) and for the constrained case in Fig. 4(b). The choice $M = 0$ corresponds to the rigid, ideally plastic limit. The ratio $\bar{p}/\bar{p}(l=0)$ increases with increasing M, except for small l/h in the unconstrained case. A comparison with the numerical solution for large aspect ratio is provided in Appendix A.

4. Shear problem

The strain gradient viscoplasticity theory of Section 2 is now specialised to a one-dimensional version of the shear problem sketched in Fig. 1(b). A

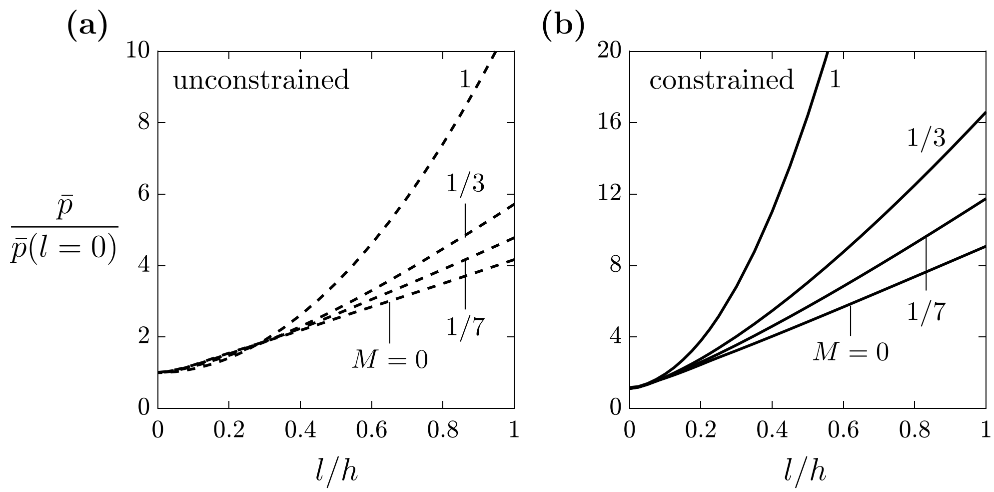

Fig. 4: Axisymmetric compression problem. Asymptotic solution for large aspect ratio $a/h \gg 1$ for the average pressure $\bar{p}$ normalised by the conventional value $\bar{p}(l = 0)$ as a function of l/h, for selected values of creep exponent M. **(a)** Unconstrained and **(b)** constrained higher-order boundary conditions.

Cartesian reference system (x, z) is introduced, with origin at the centre of the bottom face of the layer. The face of the layer at $z = 0$ is fixed, whereas a tangential velocity (in the x-direction) $\dot{u}_x = v$ is imposed on the face at $z = h$. For large aspect ratio $a/h \gg 1$, edge effects can be neglected and the problem is one-dimensional in the z-direction. The only non-zero velocity component is $\dot{u}_x$, and the only non-zero component of the strain rate tensor is the shear strain rate $\dot{\gamma} \equiv 2\dot{\varepsilon}_{xz} = \partial \dot{u}_x / \partial z$.

4.1. Numerical solution

A numerical solution for the one-dimensional shear problem $\dot{\gamma}(z)$ is obtained by making use of COMSOL Multiphysics. The equilibrium statements of Eqs. (6) reduce to a single equation $(q - \tau_{,z})_{,z} = 0$, where the symbols q

and τ are used to simplify the notation of q_{xz} and τ_{xzz}, respectively. Note that (q, τ) are the only non-zero components of the stress tensors q_{ij} and τ_{ijk} for the case of simple shear, and are related to $\dot{\gamma}$ and $\dot{\gamma}_{,z}$ via the constitutive relations of Eqs. (12).

The governing equilibrium equation is a non-linear fourth-order equation in the unknown tangential displacement $\dot{u}_x$. This equation is implemented in COMSOL Multiphysics, and quadratic finite elements are used for the numerical discretisation. The mesh again consists of 100 finite elements in the z-direction, with a finer mesh adopted near the domain boundaries; the ratio of largest to smallest element size equals 20. The boundary conditions are $\dot{u}_x = 0$ on $z = 0$ and $\dot{u}_x = v$ on $z = h$. The *constrained* higher-order boundary condition is $\dot{\gamma} = 0$ on $z = 0$ and $z = h$. In contrast, the *unconstrained* higher-order boundary condition is $\tau = 0$ on $z = 0$ and $z = h$. We can state immediately that the unconstrained higher-order boundary condition reduces the problem to the trivial case of simple shear of a conventional power law creeping solid.

The normalised velocity field $\dot{u}_x/v$ and the normalised shear strain rate $h\dot{\gamma}/v$, as obtained by the numerical solution for constrained higher-order boundary conditions, are plotted in Fig. 5 as a function of z/h, for $M = 1/7$ and for selected values of l/h. A comparison between Fig. 2(d) and Fig. 5(b) reveals that the shear strain rate gradient at the layer/substrate interfaces is much larger for the compressed sample than for the sheared sample. Moreover, in compression, a shear strain rate gradient develops at the mid-plane, unlike the shear case. For the choice of unconstrained $\dot{\gamma}$ at the boundaries, the solution is one of uniform shear strain rate, and is labelled $l/h = 0$ in Fig. 5.

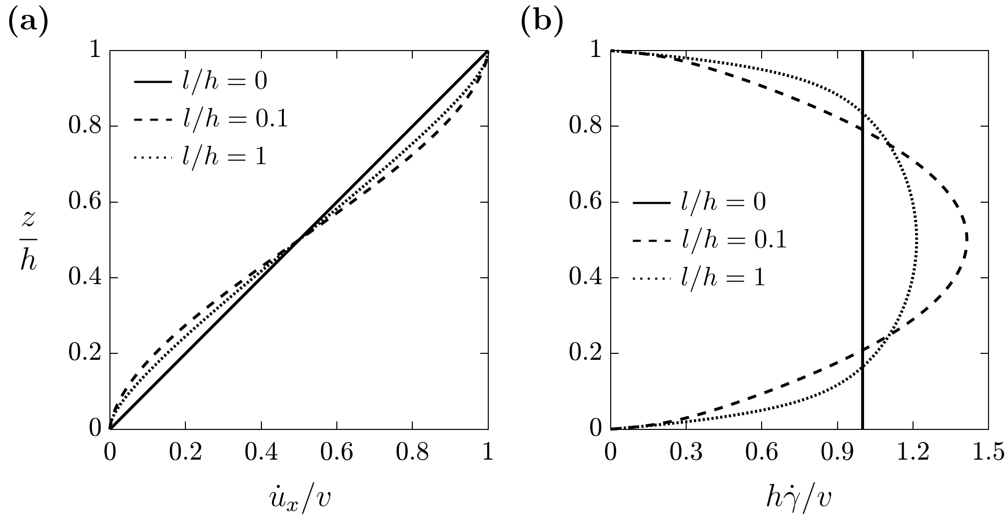

Fig. 5: Shear problem. Numerical solution for constrained higher-order boundary condition: **(a)** $\dot{u}_x/v$ and **(b)** $h\dot{\gamma}/v$ as a function of z/h for $M = 1/7$ and for selected values of l/h. The solution for $l/h = 0$ corresponds to the solution of the conventional viscoplastic problem or, equivalently, of the strain-gradient viscoplastic problem with an unconstrained higher-order boundary condition.

The traction T_x, denoted by T for brevity, is plotted as a function of l/h in Fig. 6(a). Predictions are given for selected values of M. The traction increases with increasing l/h, and increases with increasing M except for small values of l/h. The ratio $T/T(l = 0)$, quantifying the size effect in shear, is given in Fig. 6(b), again as a function of l/h and for selected values of M. The size effect increases with increasing l/h and with increasing M, as for constrained compression. A comparison of the numerical solution with an upper bound analytical solution for an assumed velocity field is presented in Appendix B.

The differences in the profiles of shear strain rate through the thickness of

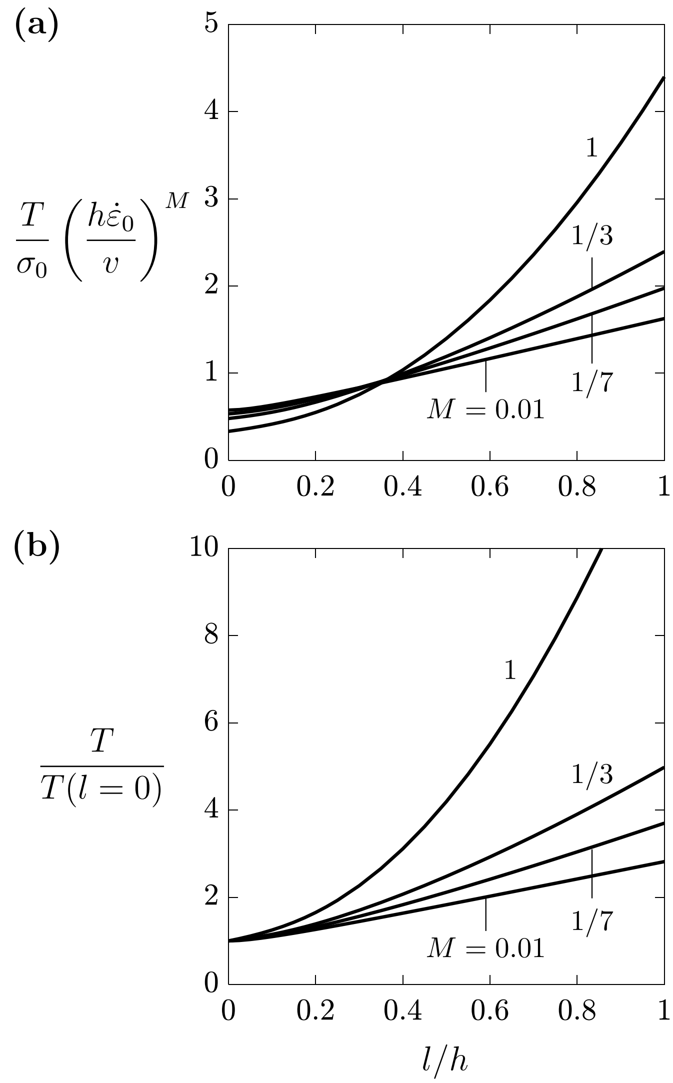

Fig. 6: Shear problem. Numerical solution for **(a)** $(T/\sigma_0)(h\dot{\varepsilon}_0/v)^M$ and **(b)** $T/T(l=0)$ as a function of l/h and for selected values of M, in the case of constrained $\dot{\gamma}$ at the boundaries.

the layer in axisymmetric compression and in shear explain why the predicted size effect in compression is larger than in shear. For example, given $M = 1/7$ and $l/h = 1$, and for constrained higher-order boundary conditions, a three times larger size effect in compression than in shear is observed by comparing Fig. 4(b) and Fig. 6(b). A quantitative comparison between size effects revealed by recent experiments of Stallard et al. (2023) and predicted by the strain gradient based creep theory for compressed and sheared constrained lithium layers is now given.

5. Comparison with experiments on lithium

Axisymmetric compression data for lithium given by Stallard et al. (2023) are plotted in the form of of $\bar{p}(h\dot{\varepsilon}_0/v)^M(h/a)^{M+1}$ versus thickness h in Fig. 7(a). Stallard et al. (2023) compressed lithium spheres of initial diameter D until the lithium specimen could be adequately described by a circular cylinder of radius a and height h, and they plotted $\bar{p}$ versus a/h. Volume conservation demands that the height h is directly related to the aspect ratio a/h by $h/D = (1/6)^{1/3}(h/a)^{2/3}$. Consequently, a plot of $\bar{p}$ versus a/h can be transformed into a plot of $\bar{p}$ versus h for any sample of initial diameter D. We fit the strain gradient theory with constrained higher-order boundary conditions to these data in order to determine the material length scale l. Predictions are given for selected values of l in Fig. 7(a), with $\sigma_0 = 1\,\text{MPa}$ and $M = 1/6.55$ (Masias et al., 2019; Fincher et al., 2020). Best agreement with experiments is obtained for a value of l on the order of $3\,\mu\text{m}$.

Shear data presented in Stallard et al. (2023) are plotted in terms of $T(h\dot{\varepsilon}_0/v)^M$ as a function of h in Fig. 7(b). Numerical curves for the con-

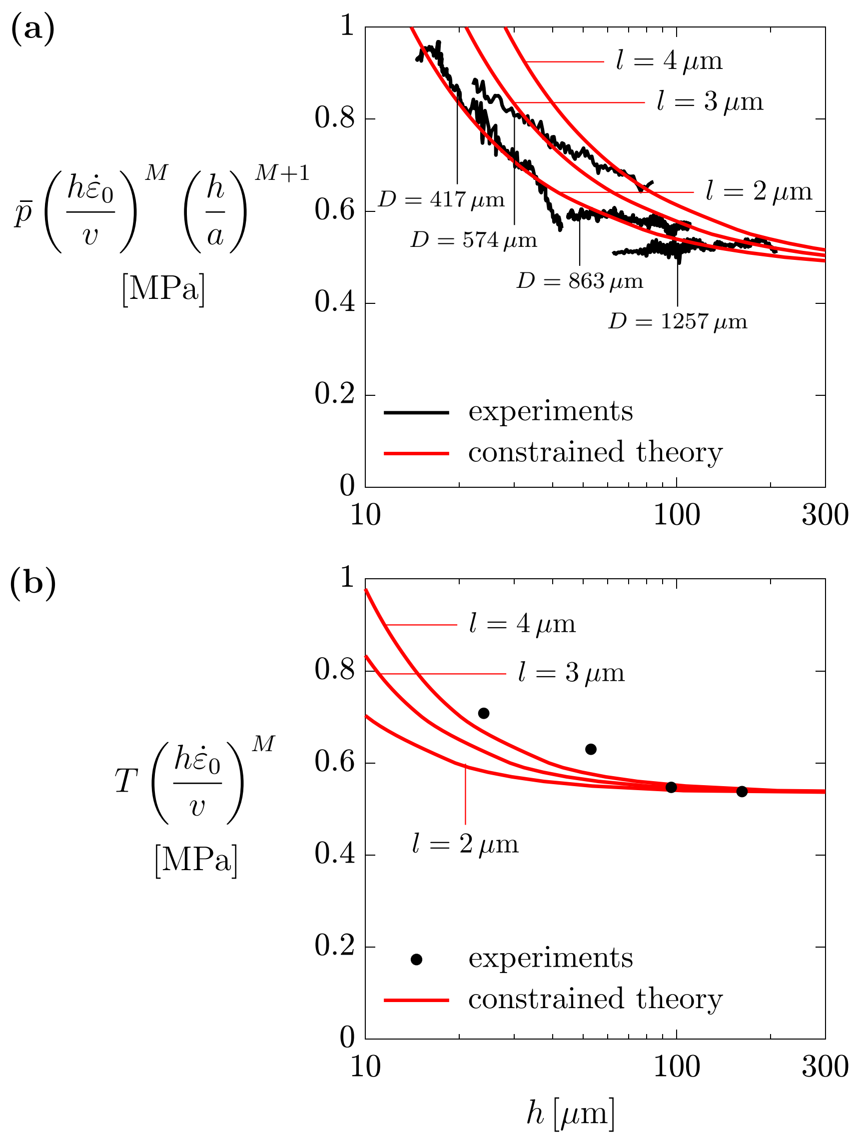

Fig. 7: Comparison between experimental results and numerical solution of the strain gradient theory with constrained higher-order boundary conditions for **(a)** axisymmetric compression and **(b)** simple shear. Predictions are given for selected values of l. Both experimental results and numerical solution assume a creep exponent $M = 1/6.55$.

strained creep problem, obtained again for $\sigma_0 = 1\,\mathrm{MPa}$ and $M = 1/6.55$, are included in Fig. 7(b). The solution of the constrained creep problem slightly underestimates the measured shear response, for the choice $l = 3\,\mu\mathrm{m}$ that gave the best fit to the compression data. It is anticipated that a better fit to both the compression and shear data can be achieved by the use of a more sophisticated gradient theory that involves more than a single length scale, see for example Smyshlyaev and Fleck (1996). Begley and Hutchinson (1998) have shown that more than one material length scale is needed in order to predict the observed size effect in shear tests and in indentation. Specifically, they showed that indentation gives rise to stretch gradients whereas shear tests give rise to rotation gradients, that is, curvature. Different material length scales can accompany these two modes of deformation.

6. Concluding remarks

The present study highlights the fact that size effects are observed in power law creeping metals and alloys in addition to the regime of rate independent plasticity. The underlying physical mechanisms remain to be resolved but it is noted here that the material length scale l that is needed to fit strain gradient plasticity models to observed size effects is on the order of $3\,\mu\mathrm{m}$. It is conjectured that the relevant material length scale that dictates the value of l is the steady-state subgrain size λ_{ss}, which is sensitive to the ratio of steady-state flow stress σ_{ss} to shear modulus G. For lithium tested at $\dot{\varepsilon}_{\mathrm{ss}} = 10^{-3}\,\mathrm{s}^{-1}$, σ_{ss} is on the order of $1\,\mathrm{MPa}$ such that $\sigma_{\mathrm{ss}}/G = 3 \times 10^{-4}$. The steady-state subgrain size λ_{ss} is about $15\,\mu\mathrm{m}$ for $\sigma_{\mathrm{ss}}/G = 3 \times 10^{-4}$ in the case of aluminium and 304 stainless steel, see Figs. 18 and 19 of the review article by Kassner and Pérez-Prado (2000). Precise values of λ_{ss} for lithium have not been reported in the literature to the author's knowledge. There remains the need to relate the material length scale l to the evolving microstructure in the creep regime. An initial attempt to generate a macroscopic gradient theory for a periodic composite microstructure made from rate independent, elasto-plastic solids was achieved by the pioneering study of Triantafyllidis and Bardenhagen (1996).

The analysis of the present study reveals that the dominant gradient in axisymmetric compression is the gradient of shear strain rate through the thickness of the specimen. Such a gradient of shear strain rate exists for simple shear of the thin layer when subjected to fully constrained higher-order boundary conditions. In contrast, unconstrained higher-order boundary conditions give no predicted size effect for simple shear and only a mild size effect for axisymmetric compression. Finally, the analytical models give useful physical insight into the dominant terms of the velocity field in both axisymmetric compression and simple shear. The analytical model for axisymmetric compression reveals that the size effect can be decoupled in a multiplicative manner from the effect of plastic constraint associated with specimen aspect ratio a/h.

Acknowledgements

This work was aided by the Faraday Institution projects "FutureCat" with grant no. FIRG017 and "Degradation" under grant no. FIRG001 and FIRG024. The authors are also grateful for support from the European Research Council project MULTILAT, with grant no. 669764. The authors are

grateful to Dr. Joe Stallard of Cambridge University Engineering Department for useful discussions and access to his published data.

Appendix A. Analytical solution for axisymmetric compression

An analytic solution for the axisymmetric compression problem of Section 3 is obtained for the assumed velocity field of Eqs. (13). The non-vanishing components of the strain rate tensor follow directly as:

$$\dot{\varepsilon}_{rr} \equiv \frac{\partial \dot{u}_r}{\partial r} = \frac{v}{h}\left[C_1\bar{z}(1-\bar{z}) + C_2\bar{z}^2(1-\bar{z})^2 + C_3\bar{z}^3(1-\bar{z})^3\right] \tag{A.1a}$$

$$\dot{\varepsilon}_{\theta\theta} \equiv \frac{\dot{u}_r}{r} = \dot{\varepsilon}_{rr} \tag{A.1b}$$

$$\dot{\varepsilon}_{zz} \equiv \frac{\partial \dot{u}_z}{\partial z} = -2\dot{\varepsilon}_{rr} \tag{A.1c}$$

$$2\dot{\varepsilon}_{rz} \equiv \frac{\partial \dot{u}_r}{\partial z} + \frac{\partial \dot{u}_z}{\partial r} = \frac{v}{h}\bar{a}\hat{r}(1-2\bar{z})\left[C_1 + 2C_2\bar{z}(1-\bar{z}) + 3C_3\bar{z}^2(1-\bar{z})^2\right] \tag{A.1d}$$

The incompressibility constraint $\dot{\varepsilon}_{kk} = 0$ is satisfied identically by the chosen velocity field. Note that only the shear strain rate $\dot{\varepsilon}_{rz}$ depends on r. The non-vanishing components of the strain rate tensor gradient are given by:

$$\dot{\varepsilon}_{rr,z} \equiv \frac{\partial \dot{\varepsilon}_{rr}}{\partial z} = \frac{v}{h^2}(1-2\bar{z})\left[C_1 + 2C_2\bar{z}(1-\bar{z}) + 3C_3\bar{z}^2(1-\bar{z})^2\right] \tag{A.2a}$$

$$\dot{\varepsilon}_{\theta\theta,z} \equiv \frac{\partial \dot{\varepsilon}_{\theta\theta}}{\partial z} = \dot{\varepsilon}_{rr,z} \tag{A.2b}$$

$$\dot{\varepsilon}_{zz,z} \equiv \frac{\partial \dot{\varepsilon}_{zz}}{\partial z} = -2\dot{\varepsilon}_{rr,z} \tag{A.2c}$$

$$2\dot{\varepsilon}_{rz,r} \equiv 2\frac{\partial \dot{\varepsilon}_{rz}}{\partial r} = \dot{\varepsilon}_{rr,z} \tag{A.2d}$$

$$\dot{\varepsilon}_{rz,z} \equiv \frac{\partial \dot{\varepsilon}_{rz}}{\partial z} = \frac{v}{h^2}\bar{a}\hat{r}\left[-C_1 + C_2(6\bar{z}^2 - 6\bar{z} + 1) + 3C_3\bar{z}(1-\bar{z})(5\bar{z}^2 - 5\bar{z} + 1)\right] \tag{A.2e}$$

$$2\dot{\varepsilon}_{\theta z,\theta} \equiv 2\frac{\dot{\varepsilon}_{rz}}{r} = \dot{\varepsilon}_{rr,z} \tag{A.2f}$$

Consequently, the only component of $\dot{\varepsilon}_{ij,k}$ that depends upon r is the shear strain rate gradient in the z-direction, $\dot{\varepsilon}_{rz,z}$.

The velocity field given by Eqs. (13) is chosen to be of a form that satisfies the boundary conditions $\dot{u}_z = 0$ on $z = 0$ and $\dot{u}_r = 0$ on both $z = 0$ and $z = h$. The prescribed velocity $\dot{u}_z = -v$ on the upper surface $z = h$ imposes an algebraic constraint between the scaling factors C_1, C_2 and C_3 such that

$$C_3 = 70\left(1 - \frac{C_1}{3} - \frac{C_2}{15}\right) \tag{A.3}$$

Note that $\dot{\varepsilon}_{rr} = \dot{\varepsilon}_{\theta\theta} = \dot{\varepsilon}_{zz} = 0$ on $z = 0$ and on $z = h$ for any choice of C_1 and C_2; this is a direct consequence of the no-slip boundary condition and incompressibility constraint. There remains choice in the assumed higher-order boundary condition on $z = 0$ and $z = h$, as follows. The kinematically constrained higher-order boundary condition demands that $\dot{\varepsilon}_{rz} = 0$, while the unconstrained higher-order boundary condition corresponds to a vanishing higher-order traction t_{rz}. In the constrained case, C_1 vanishes from Eq. (A.1d). Alternatively, in the unconstrained case, a vanishing value of t_{rz} on the upper and lower boundaries implies that $\dot{\varepsilon}_{rz,z} = 0$ via Eqs. (7b) and (12b); consequently, C_1 equals C_2, as demanded by Eq. (A.2e).

The effective strain rate in Eq. (9) is written in terms of the strain rate components in Eqs. (A.1) and of the strain rate gradient components in Eqs. (A.2). Define the creep potential of the body Φ as the volume integral of the creep potential $U_{\mathrm{p}}(\dot{E}_{\mathrm{p}})$ in Eq. (10) over the body. Consequently, Φ is of the form

$$\Phi = (\pi a^2 h)\frac{\sigma_0\dot{\varepsilon}_0}{M+1}\left(\frac{v}{\dot{\varepsilon}_0 h}\right)^{M+1} f_{\rm c}\left(C_2, M, \bar{l}, \bar{a}\right) \tag{A.4}$$

where $\bar{l} = l/h$ and the non-dimensional function $f_{\rm c}$ reads

$$\begin{aligned} f_{\rm c} = 2\int_0^1\int_0^1 \Bigg\{ & 4\left[C_1\bar{z}(1-\bar{z}) + C_2\bar{z}^2(1-\bar{z})^2 + C_3\bar{z}^3(1-\bar{z})^3\right]^2 \\ & + \frac{\bar{a}^2\hat{r}^2 + 14\bar{l}^2}{3}(1-2\bar{z})^2\left[C_1 + 2C_2\bar{z}(1-\bar{z}) + 3C_3\bar{z}^2(1-\bar{z})^2\right]^2 \\ + \frac{4\bar{a}^2\bar{l}^2\hat{r}^2}{3} & \left[-C_1 + C_2(6\bar{z}^2 - 6\bar{z} + 1) + 3C_3\bar{z}(1-\bar{z})(5\bar{z}^2 - 5\bar{z} + 1)\right]^2 \Bigg\}^{\frac{M+1}{2}} \hat{r}\mathrm{d}\hat{r}\mathrm{d}\bar{z} \end{aligned} \tag{A.5}$$

Recall that C_3 depends upon C_1 and C_2 via Eq. (A.3); moreover, $C_1 = 0$ in the constrained case and $C_1 = C_2$ in the unconstrained case. The value of the remaining integration constant C_2 is obtained by minimisation of the rate potential of the body (Fleck and Willis, 2009; Niordson and Hutchinson, 2011). Given values of M, $\bar{l}$ and $\bar{a}$, minimisation of $f_{\rm c}$ with respect to C_2 gives the optimal value of C_2.[2] The corresponding value of Φ, called $\Phi_{\rm min}$, is used to determine the average pressure $\bar{p}$ such that

$$\bar{p} = \frac{1}{\pi a^2}\frac{\partial \Phi_{\rm min}}{\partial v} = \sigma_0\left(\frac{v}{h\dot{\varepsilon}_0}\right)^M \min_{C_2}\left\{f_{\rm c}\left(C_2, M, \bar{l}, \bar{a}\right)\right\} \tag{A.6}$$

The non-dimensional average pressure $(\bar{p}/\sigma_0)(h\dot{\varepsilon}_0/v)^M$, given by Eq. (A.6), is plotted in Fig. A.1(a) as a function of l/h, for $M = 1/7$ and for selected values of a/h. For comparison purposes, the numerical solution given previously in Fig. 3(a) is included in Fig. A.1(a). Excellent agreement is observed between

[2]To find the optimal value of C_2 for given values of M, $\bar{l}$ and $\bar{a}$, the function $f_{\rm c}$ is numerically evaluated in MATLAB, version R2020A, for each integer value of C_2 in the range $-1000 < C_2 < 1000$. The function `vpaintegral` is used for numerical integration.

analytical and numerical solutions. We emphasise that the analytical solution is an upper bound to the numerical solution, and slightly overpredicts the numerical solution by less than 10%.

Strain gradient effects are absent for the choice $l = 0$, conventional rate dependent plasticity is recovered and no higher-order boundary condition can be imposed. In this limit it is necessary to minimise f_c with respect to both C_1 and C_2. Therefore, for conventional rate dependent plasticity:

$$\bar{p}(l=0) = \sigma_0 \left(\frac{v}{h\dot{\varepsilon}_0}\right)^M \min_{C_1, C_2} \left\{ f_\mathrm{c}\left(C_1, C_2, M, \bar{l}=0, \bar{a}\right)\right\} \tag{A.7}$$

The prediction of Eq. (A.7) and the finite element solution for $l = 0$ are plotted in Fig. A.2 as a function of a/h and for selected values of M. The upper bound analytical solution overpredicts the numerical solution by less than 8%, and its accuracy increases with increasing M. For completeness, the viscous analytical solution of Cheung and Cebon (1997) for the compression of a thin power law creeping film is included in Fig. A.2. Their formula reads

$$\frac{\bar{p}}{\sigma_0} = \frac{1}{M+3}\left(\frac{2}{\sqrt{3}}\right)^{M+1}\left(\frac{2M+1}{2M}\right)^M \left(\frac{v}{h\dot{\varepsilon}_0}\right)^M \left(\frac{a}{h}\right)^{M+1} \tag{A.8}$$

and converges to the numerical solution for $l = 0$ at large aspect ratio a/h. Convergence with respect to a/h is attained more quickly as M is increased.

The effect of strain rate gradients upon the required force for axisymmetric compression of the sandwich layer with higher-order constraint can be quantified by taking the ratio of Eqs. (A.6) and (A.7):

$$\frac{\bar{p}}{\bar{p}(l=0)} = \frac{\min\limits_{C_2}\left\{f_\mathrm{c}\left(C_2, M, \bar{l}, \bar{a}\right)\right\}}{\min\limits_{C_1, C_2}\left\{f_\mathrm{c}\left(C_1, C_2, M, \bar{l}=0, \bar{a}\right)\right\}} \tag{A.9}$$

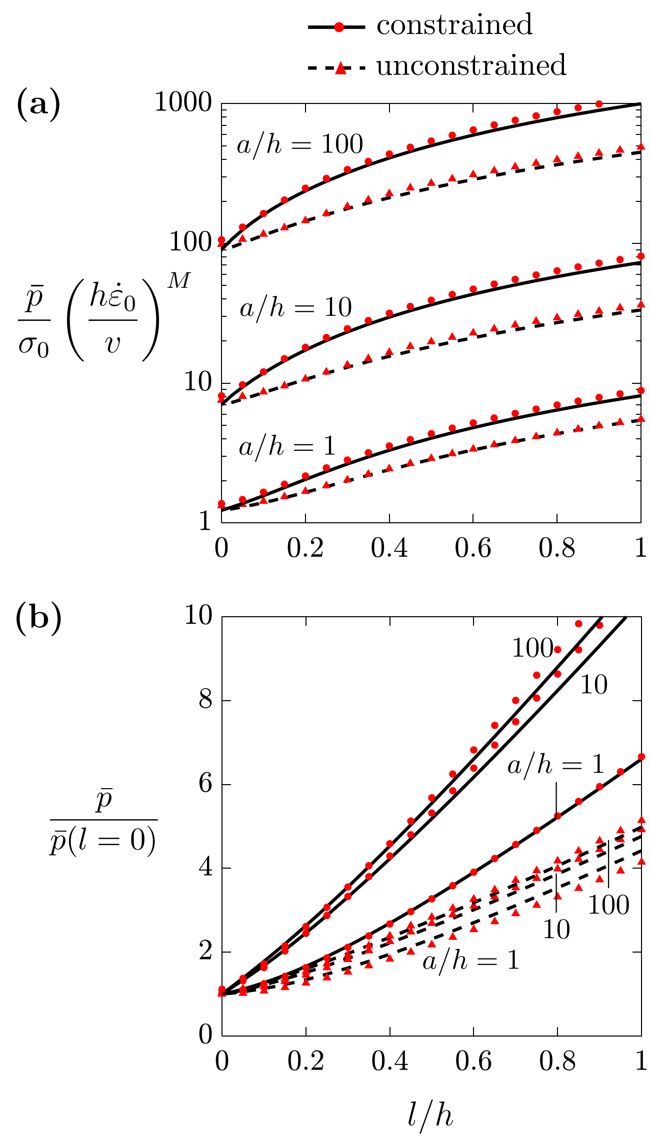

Fig. A.1: Axisymmetric compression problem. Numerical solution (black lines) and analytical solution (red data points) for constrained and unconstrained higher-order boundary conditions: **(a)** $(\bar{p}/\sigma_0)(h\dot{\varepsilon}_0/v)^M$ and **(b)** $\bar{p}/\bar{p}(l=0)$ as a function of l/h for $M = 1/7$ and for selected values of a/h.

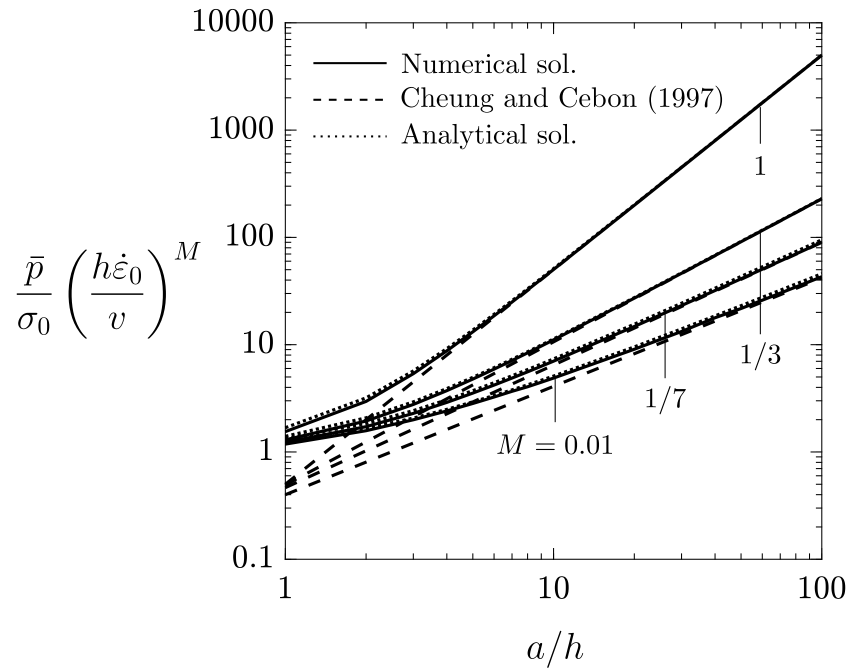

Fig. A.2: Non-dimensional average pressure $(\bar{p}/\sigma_0)(h\dot{\varepsilon}_0/v)^M$ as a function of a/h for conventional power law creep: the viscous solution Eq. (A.8) of Cheung and Cebon (1997), the numerical solution of Section 3 for $l = 0$ and the analytical upper bound solution Eq. (A.7).

This pressure ratio is plotted in Fig. A.1(b) as a function of l/h, for the choice $M = 1/7$ and for selected values of aspect ratio a/h, alongside the numerical solution that is taken from Fig. 3(b).

Now consider the case of large aspect ratio, $\bar{a} = a/h \gg 1$. Except for small values of $\hat{r} = r/a \ll 1$, the shear strain rate in Eq. (A.1d) and the shear strain rate gradient in Eq. (A.2e) dominate all other components of the strain rate tensor and of the gradient of the strain rate tensor, respectively. Therefore, the effective strain rate in Eq. (9) can be simplified by including only the contributions from Eqs. (A.1d) and (A.2e). Consequently, Eq. (A.4) reduces to

$$\Phi = (\pi a^2 h)\frac{\sigma_0\dot{\varepsilon}_0}{M+1}\left(\frac{v}{\dot{\varepsilon}_0 h}\right)^{M+1}\frac{\bar{a}^{M+1}}{M+3}\,g_{\mathrm{c}}\left(C_2, M, \bar{l}\right) \tag{A.10}$$

where

$$\begin{aligned} g_{\mathrm{c}} = 2\int_0^1 &\left\{\frac{1}{3}(1-2\bar{z})^2\left[C_1 + 2C_2\bar{z}(1-\bar{z}) + 3C_3\bar{z}^2(1-\bar{z})^2\right]^2\right. \\ &+ \left.\frac{4\bar{l}^2}{3}\left[-C_1 + C_2(6\bar{z}^2 - 6\bar{z} + 1) + 3C_3\bar{z}(1-\bar{z})(5\bar{z}^2 - 5\bar{z} + 1)\right]^2\right\}^{\frac{M+1}{2}}\mathrm{d}\bar{z} \end{aligned} \tag{A.11}$$

As before, C_3 is given by Eq. (A.3), C_1 vanishes in the constrained case and C_1 equals C_2 in the unconstrained case. For any specified values of M and $\bar{l}$, minimisation of g_{c} with respect to C_2 gives the optimal value of C_2. The corresponding value of Φ, called $\Phi_{\min}$, gives the average pressure $\bar{p}$ such that

$$\bar{p} = \frac{1}{\pi a^2}\frac{\partial \Phi_{\min}}{\partial v} = \sigma_0\left(\frac{v}{h\dot{\varepsilon}_0}\right)^{M}\frac{\bar{a}^{M+1}}{M+3}\min_{C_2}\left\{g_{\mathrm{c}}\left(C_2, M, \bar{l}\right)\right\} \tag{A.12}$$

It is clear from Eq. (A.12) that the contribution of $\bar{a}$ and of $\bar{l}$ upon $\bar{p}$ decouples in a multiplicative manner. Also, Eqs. (A.8) and (A.12) give the same functional form of the dependence of non-dimensional average pressure $\bar{p}$ upon aspect ratio $\bar{a}$. In the limit of a conventional, rate dependent solid, Eq. (A.7) becomes

$$\bar{p}(l=0) = \sigma_0\left(\frac{v}{h\dot{\varepsilon}_0}\right)^{M}\frac{\bar{a}^{M+1}}{M+3}\min_{C_1,C_2}\left\{g_{\mathrm{c}}\left(C_1, C_2, M, \bar{l}=0\right)\right\} \tag{A.13}$$

The pressure ratio is again defined by $\bar{p}/\bar{p}(l=0)$, and reads

$$\frac{\bar{p}}{\bar{p}(l=0)} = \frac{\min_{C_2}\left\{g_{\mathrm{c}}\left(C_2, M, \bar{l}\right)\right\}}{\min_{C_1,C_2}\left\{g_{\mathrm{c}}\left(C_1, C_2, M, \bar{l}=0\right)\right\}} \tag{A.14}$$

This ratio is plotted in Fig. 4 as a function of l/h for selected values of M, for both constrained and unconstrained higher-order boundary conditions. A comparison of Eq. (A.14) with finite element results obtained for $a/h = 10$ is given in Fig. A.3. Its accuracy is adequate for present purposes.

Appendix B. Analytical solution for shear

In order to obtain an analytical solution for the shear problem, it is convenient to introduce the Cartesian coordinate $Z = z - h/2$, with origin on the mid-plane of the sheared layer. Assume fully constrained higher-order boundary conditions such that $\dot{\gamma} = 0$ on $Z = \pm h/2$. A strain rate field $\dot{\gamma}(Z)$

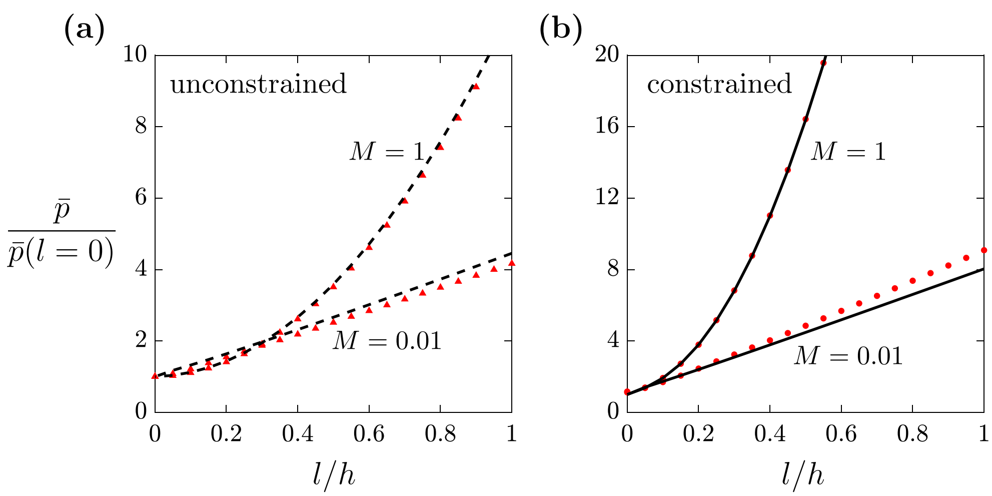

Fig. A.3: Axisymmetric compression problem. Average pressure $\bar{p}$ normalised by $\bar{p}(l = 0)$ as a function of l/h, for selected values of creep exponent M, as given by the numerical solution for $a/h = 10$ (black lines) and by the asymptotic solution for large aspect ratio $a/h \gg 1$ in Eq. (A.14) (red data points). **(a)** Unconstrained and **(b)** constrained higher-order boundary conditions.

that satisfies this requirement is

$$\frac{h\dot{\gamma}}{v} = C_1\left(\bar{Z}^2 - \frac{1}{4}\right) + C_2\left(\bar{Z}^2 - \frac{1}{4}\right)^2 \tag{B.1}$$

where $\bar{Z} = Z/h$ and C_1 and C_2 are unknown integration constants. Integration gives

$$\frac{\dot{u}_x}{v} = C_1\left(\frac{\bar{Z}^3}{3} - \frac{\bar{Z}}{4}\right) + C_2\left(\frac{\bar{Z}^5}{5} - \frac{\bar{Z}^3}{6} + \frac{\bar{Z}}{16}\right) + C_3 \tag{B.2}$$

and symmetry requires that $\dot{u}_x/v = 1/2$ at $Z = 0$, such that $C_3 = 1/2$. The velocity boundary conditions of $\dot{u}_x = 0$ at $Z = -h/2$ and $\dot{u}_x = v$ at $Z = h/2$ require that $C_2 = 5C_1 + 30$. Consequently, the tangential velocity, shear strain rate and its gradient for the constrained case are:

$$\frac{\dot{u}_x}{v} = C_1\left(\bar{Z}^5 - \frac{\bar{Z}^3}{2} + \frac{\bar{Z}}{16}\right) + 6\bar{Z}^5 - 5\bar{Z}^3 + \frac{15}{8}\bar{Z} + \frac{1}{2} \tag{B.3a}$$

$$\frac{h\dot{\gamma}}{v} = C_1\left(5\bar{Z}^4 - \frac{3}{2}\bar{Z}^2 + \frac{1}{16}\right) + 30\bar{Z}^4 - 15\bar{Z}^2 + \frac{15}{8} \tag{B.3b}$$

$$\frac{h^2\dot{\gamma}_{,z}}{v} = C_1\left(20\bar{Z}^3 - 3\bar{Z}\right) + 120\bar{Z}^3 - 30\bar{Z} \tag{B.3c}$$

The effective strain rate, as defined in Eq. (9), reduces to $\dot{E}_{\mathrm{p}}^2 = \left(\dot{\gamma}^2 + l^2\dot{\gamma}_{,z}^2\right)/3$.

The creep potential $U_{\mathrm{p}}(\dot{E}_{\mathrm{p}})$ in Eq. (10) is used to obtain the rate potential per unit length in the x-direction and per unit depth, $\Phi = \int_{-h/2}^{h/2} U_{\mathrm{p}}(\dot{E}_{\mathrm{p}})\,\mathrm{d}Z$, and consequently

$$\Phi = h\frac{\sigma_0\dot{\varepsilon}_0}{M+1}\left(\frac{v}{\dot{\varepsilon}_0 h}\right)^{M+1} g_{\mathrm{s}}\left(C_1, M, \bar{l}\right) \tag{B.4}$$

where $\bar{l} = l/h$ and

$$g_{\mathrm{s}} = \int_{-1/2}^{1/2}\left\{\frac{1}{3}\left[C_1\left(5\bar{Z}^4 - \frac{3}{2}\bar{Z}^2 + \frac{1}{16}\right) + 30\bar{Z}^4 - 15\bar{Z}^2 + \frac{15}{8}\right]^2 + \frac{\bar{l}^2}{3}\left[C_1\left(20\bar{Z}^3 - 3\bar{Z}\right) + 120\bar{Z}^3 - 30\bar{Z}\right]^2\right\}^{\frac{M+1}{2}}\mathrm{d}\bar{Z} \tag{B.5}$$

The function g_s is minimised numerically with respect to C_1 and the corresponding minimum value of Φ is denoted as Φ_min. The shear stress σ_{xz}, corresponding to the traction T_x at $Z = \pm h/2$, see Eq. (7a), is denoted as T for convenience of notation and reads

$$T = \frac{\partial \Phi_\mathrm{min}}{\partial v} = \sigma_0 \left(\frac{v}{h \dot{\varepsilon}_0} \right)^M \min_{C_1} \left\{ g_\mathrm{s} \left(C_1, M, \bar{l} \right) \right\} \tag{B.6}$$

This is plotted in non-dimensional fashion in Fig. B.1(a) as a function of l/h, for selected values of M, alongside the numerical solution previously given in Fig. 6(a). The analytical solution is an upper bound to the numerical solution and overestimates the latter by less than 9%. The accuracy of the analytical solution increases with increasing M, consistent with the case of compression, as noted above.

Now consider unconstrained higher-order boundary conditions. The shear strain rate is uniform, $\dot{\gamma} = v/h$; consequently, the gradient theory reduces to the conventional theory for a power law creeping solid and the shear traction is

$$T(l = 0) = \sigma_0 \left(\frac{v}{h \dot{\varepsilon}_0} \right)^M \left(\frac{\sqrt{3}}{3} \right)^{M+1} \tag{B.7}$$

Finally, the ratio of Eq. (B.6) to Eq. (B.7), which gives a measure of the strengthening in shear due to the constraint of vanishing shear strain rate at the boundaries in the strain gradient theory, is

$$\frac{T}{T(l = 0)} = \left(\frac{\sqrt{3}}{3} \right)^{-M-1} \min_{C_1} \left\{ g_\mathrm{s} \left(C_1, M, \bar{l} \right) \right\} \tag{B.8}$$

This ratio is plotted in Fig. B.1(b), alongside the numerical solution of Fig. 6(b): agreement is again adequate.

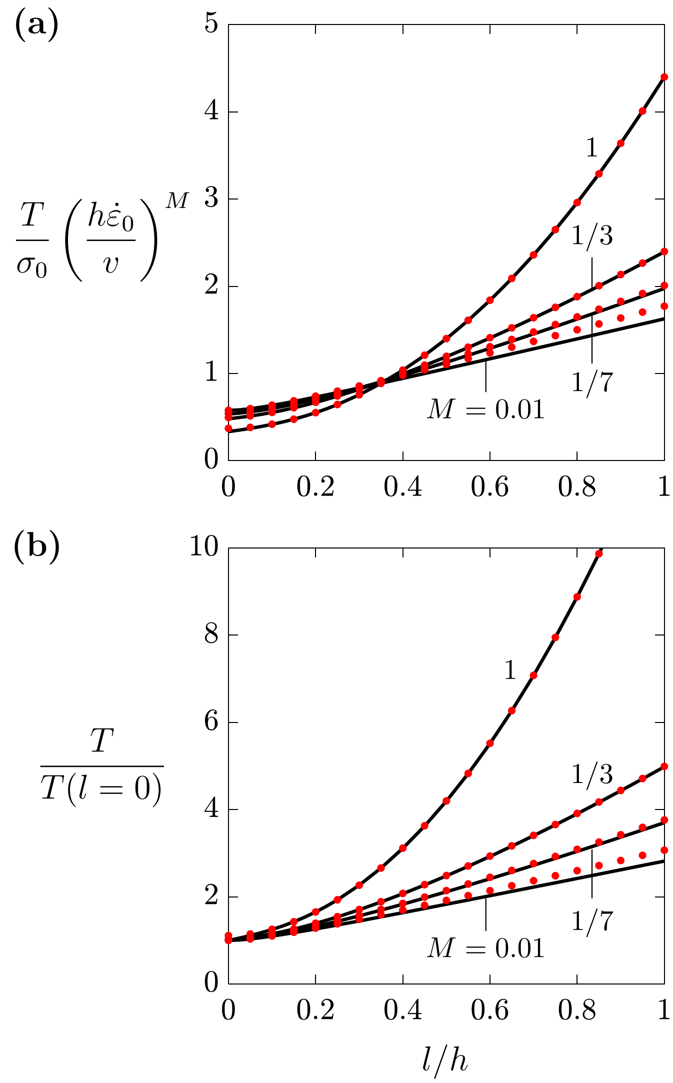

Fig. B.1: Shear problem. Numerical solution (solid lines) and analytical solution (red data points) for **(a)** $(T/\sigma_0)(h\dot{\varepsilon}_0/v)^M$ and **(b)** $T/T(l=0)$ as a function of l/h, for selected values of M. The constrained higher-order boundary condition $\dot{\gamma} = 0$ is assumed.

References

Ashby, M.F., 1970. The deformation of plastically non-homogeneous materials. The Philosophical Magazine: A Journal of Theoretical Experimental and Applied Physics 21, 399–424.

Begley, M.R., Hutchinson, J.W., 1998. The mechanics of size-dependent indentation. Journal of the Mechanics and Physics of Solids 46, 2049–2068.

Cheng, E.J., Sharafi, A., Sakamoto, J., 2017. Intergranular Li metal propagation through polycrystalline $Li_{6.25}Al_{0.25}La_3Zr_2O_{12}$ ceramic electrolyte. Electrochimica Acta 223, 85–91.

Cheung, C.Y., Cebon, D., 1997. Thin film deformation behavior of power-law creeping materials. Journal of Engineering Mechanics 123, 1138–1152.

Dahlberg, C.F.O., Ortiz, M., 2019. Fractional strain-gradient plasticity. European Journal of Mechanics - A/Solids 75, 348–354.

Danas, K., Deshpande, V.S., Fleck, N.A., 2010. Compliant interfaces: A mechanism for relaxation of dislocation pile-ups in a sheared single crystal. International Journal of Plasticity 26, 1792–1805.

Fincher, C.D., Ojeda, D., Zhang, Y., Pharr, G.M., Pharr, M., 2020. Mechanical properties of metallic lithium: from nano to bulk scales. Acta Materialia 186, 215–222.

Fleck, N.A., Muller, G.M., Ashby, M.F., Hutchinson, J.W., 1994. Strain gradient plasticity: Theory and experiment. Acta Metallurgica et Materialia 42, 475–487.

Fleck, N.A., Willis, J.R., 2009. A mathematical basis for strain-gradient plasticity theory. Part II: Tensorial plastic multiplier. Journal of the Mechanics and Physics of Solids 57, 1045–1057.

Herbert, E.G., Hackney, S.A., Thole, V., Dudney, N.J., Phani, P.S., 2018. Nanoindentation of high-purity vapor deposited lithium films: A mechanistic rationalization of diffusion-mediated flow. Journal of Materials Research 33, 1347–1360.

Hutchinson, J.W., Fleck, N.A., 1997. Strain gradient plasticity. Advances in Applied Mechanics 33, 295–361.

Iliev, S.P., Chen, X., Pathan, M.V., Tagarielli, V.L., 2017. Measurements of the mechanical response of indium and of its size dependence in bending and indentation. Materials Science and Engineering: A 683, 244–251.

Janek, J., Zeier, W.G., 2016. A solid future for battery development. Nature Energy 1, 1–4.

Kasemchainan, J., Zekoll, S., Spencer Jolly, D., Ning, Z., Hartley, G.O., Marrow, J., Bruce, P.G., 2019. Critical stripping current leads to dendrite formation on plating in lithium anode solid electrolyte cells. Nature Materials 18, 1105–1111.

Kassner, M.E., Pérez-Prado, M.T., 2000. Five-power-law creep in single phase metals and alloys. Progress in Materials Science 45, 1–102.

Kazyak, E., Garcia-Mendez, R., LePage, W.S., Sharafi, A., Davis, A.L., Sanchez, A.J., Chen, K.H., Haslam, C., Sakamoto, J., Dasgupta, N.P., 2020.

Li penetration in ceramic solid electrolytes: *Operando* microscopy analysis of morphology, propagation, and reversibility. Matter 2, 1025–1048.

Kuroda, M., Needleman, A., 2019. A simple model for size effects in constrained shear. Extreme Mechanics Letters 33, 100581.

Kuroda, M., Needleman, A., 2023. Non-quadratic strain gradient plasticity theory and size effects in constrained shear. Journal of Applied Mechanics 90, 121004.

Kuroda, M., Tvergaard, V., Needleman, A., 2021. Constraint and size effects in confined layer plasticity. Journal of the Mechanics and Physics of Solids 149, 104328.

LePage, W.S., Chen, Y., Kazyak, E., Chen, K.H., Sanchez, A.J., Poli, A., Arruda, E.M., Thouless, M.D., Dasgupta, N.P., 2019. Lithium mechanics: roles of strain rate and temperature and implications for lithium metal batteries. Journal of The Electrochemical Society 166, A89–A97.

Masias, A., Felten, N., Garcia-Mendez, R., Wolfenstine, J., Sakamoto, J., 2019. Elastic, plastic, and creep mechanical properties of lithium metal. Journal of Materials Science 54, 2585–2600.

Mu, Y., Hutchinson, J.W., Meng, W.J., 2014. Micro-pillar measurements of plasticity in confined Cu thin films. Extreme Mechanics Letters 1, 62–69.

Mu, Y., Zhang, X., Hutchinson, J.W., Meng, W.J., 2016. Dependence of confined plastic flow of polycrystalline Cu thin films on microstructure. MRS Communications 6, 289–294.

Mukherjee, D., Hao, S., Shearing, P.R., McMeeking, R.M., Fleck, N.A., Deshpande, V.S., 2023. Ingress of Li into solid electrolytes: Cracking and sparsely filled cracks. Small Structures , 2300022.

Ning, Z., Jolly, D.S., Li, G., De Meyere, R., Pu, S.D., Chen, Y., Kasemchainan, J., Ihli, J., Gong, C., Liu, B., et al., 2021. Visualizing plating-induced cracking in lithium-anode solid-electrolyte cells. Nature Materials 20, 1121–1129.

Ning, Z., Li, G., Melvin, D.L.R., Chen, Y., Bu, J., Spencer-Jolly, D., Liu, J., Hu, B., Gao, X., Perera, J., et al., 2023. Dendrite initiation and propagation in lithium metal solid-state batteries. Nature 618, 287–293.

Niordson, C.F., Hutchinson, J.W., 2011. Basic strain gradient plasticity theories with application to constrained film deformation. Journal of Mechanics of Materials and Structures 6, 395–416.

Sargent, P.M., Ashby, M.F., 1984. Deformation mechanism maps for alkali metals. Scripta Metallurgica 18, 145–150.

Shishvan, S.S., Fleck, N.A., McMeeking, R.M., Deshpande, V.S., 2020. Growth rate of lithium filaments in ceramic electrolytes. Acta Materialia 196, 444–455.

Shu, J.Y., Fleck, N.A., Van der Giessen, E., Needleman, A., 2001. Boundary layers in constrained plastic flow: comparison of nonlocal and discrete dislocation plasticity. Journal of the Mechanics and Physics of Solids 49, 1361–1395.

Smyshlyaev, V.P., Fleck, N.A., 1996. The role of strain gradients in the grain size effect for polycrystals. Journal of the Mechanics and Physics of Solids 44, 465–495.

Stallard, J.C., Vema, S., Grey, C.P., Deshpande, V.S., Fleck, N.A., 2023. The strength of a constrained lithium layer. Acta Materialia, to appear.

Triantafyllidis, N., Bardenhagen, S., 1996. The influence of scale size on the stability of periodic solids and the role of associated higher order gradient continuum models. Journal of the Mechanics and Physics of Solids 44, 1891–1928.

Wang, Y., Cheng, Y.T., 2017. A nanoindentation study of the viscoplastic behavior of pure lithium. Scripta Materialia 130, 191–195.

Xu, C., Ahmad, Z., Aryanfar, A., Viswanathan, V., Greer, J.R., 2017. Enhanced strength and temperature dependence of mechanical properties of Li at small scales and its implications for Li metal anodes. Proceedings of the National Academy of Sciences 114, 57–61.